Research Article

Nano Biomed Eng

Highly Sensitive Detection and Molecular Subtyping of Breast Cancer Cells Using Machine Learning-assisted SERS Technology

Xinyu Miao[1,2,§], Lei Xu[1,2,§], Li Sun[1,2,§], Yujiao Xie[1,2✉], Jiahao Zhang[1,2], Xiawei Xu[1,2], Yue Hu[1,2], Zhouxu Zhang[1,2], Aochi Liu[1,2], Zhiwei Hou[1,2], Aiguo Wu[1,2✉], Jie Lin[1,2✉]

[1] Ningbo Key Laboratory of Biomedical Imaging Probe Materials and Technology, Laboratory of Advanced Theranostic Materials and Technology, Chinese Academy of Sciences (CAS) Key Laboratory of Magnetic Materials and Devices, Ningbo Institute of Materials Technology and Engineering, Chinese Academy of Sciences, Ningbo 315201, China

[2] Zhejiang International Cooperation Base of Biomedical Materials Technology and Application, Zhejiang Engineering Research Center for Biomedical Materials, Ningbo Cixi Institute of Biomedical Engineering, Ningbo 315300, China

[§] These authors contributed equally to this work.

✉ Corresponding authors. E-mails: Yujiao Xie, xieyujiao@nimte.ac.cn; Aiguo Wu, aiguo@nimte.ac.cn; Jie Lin, linjie@nimte.ac.cn

Received: Dec. 8, 2024; **Revised:** Jan. 4, 2025; **Accepted:** Jan. 15, 2025

Citation: X.Y. Miao, L. Xu, L. Sun, et al. Highly sensitive detection and molecular subtyping of breast cancer cells using machine learning-assisted sers technology. *Nano Biomedicine and Engineering*, 2025, 17(1): 129−142.

http://doi.org/10.26599/NBE.2025.9290113

Abstract

Breast cancer has always been a research hotspot in the medical field due to its highest incidence and mortality rates among women worldwide. However, the significant molecular heterogeneity of breast cancer presents major challenges for its diagnosis and treatment. Surface-enhanced Raman spectroscopy (SERS) has gained considerable attention for its capability in trace detection and molecular analysis. To accurately identify different breast cancer cell subtypes, constructing reliable SERS bioprobes is essential. Therefore, a specific highly expressed receptor, human epidermal growth factor receptor 2 (HER-2), was employed to explore SERS bioprobes in this study. Two bioprobes capable of targeting breast cancer cells, Au NPs@4-MBA@PDA@aHER-2 and Au NPs@4-MPY@PDA@aHER-2, were synthesized. SERS performance testing indicated that the Au NPs were able to detect and trace molecules at concentrations as low as 2×10^{-9} mol/L. Additionally, the two bioprobes exhibited good spectral stability with a relative standard deviation (RSD) of 9.58%. Moreover, by constructing a "symphonic SERS spectra" of the two bioprobes with prominent component analysis-linear discriminant analysis (PCA-LDA), the classification accuracy of distinguishing white blood cells (WBCs) and two breast cancer cell subtypes (SK-BR-3 and MDA-MB-231) reached up to 97.33%. The integration of machine learning with SERS detection provides a novel technological pathway for the early diagnosis and personalized treatment of breast cancer.

Keywords: surface-enhanced Raman spectroscopy (SERS); human epidermal growth factor receptor 2 (HER-2); breast cancer; machine learning; gold nanoparticles (Au NPs); bioprobes

Introduction

Malignant tumors pose a significant threat to global human health and are one of the leading causes of death worldwide. In China, they have become the primary cause of death in both urban and rural populations, accounting for approximately 20% of all

mortality [1]. Among them, breast cancer remains the most prevalent cancer in women globally and is the leading cause of cancer-related deaths among females. In addition, the incidence of breast cancer continues to rise in most countries and regions [2]. Early diagnosis and treatment are crucial for improving the quality of life, reducing mortality rates, and enhancing the prognosis of cancer patients [3]. Currently, breast cancer screening primarily relies on imaging techniques such as ultrasound and mammography, as well as pathological tissue biopsy that requires invasive methods like surgery or needle biopsy to obtain tumor tissue [4]. However, uncertainties associated with tumor imaging diagnoses and the invasiveness of pathological biopsies limit early detection to some extent [5]. As a result, early diagnosis of breast cancer remains an urgent challenge. Moreover, breast cancer also shows significant molecular heterogeneity [6]. Based on expression levels of various cellular receptors including estrogen receptor-positive (ER^+), progesterone receptor-positive (PR^+), human epidermal growth factor receptor 2-positive ($HER\text{-}2^+$), and triple-negative breast cancer (TNBC), it can be primarily classified into several subtypes [7]. Consequently, even patients with histologically identical tumors may respond differently to the same treatment regimen, resulting in variations in therapeutic sensitivity and prognosis [8]. This variability further highlights the need for more precise diagnostic strategies and therapeutic approaches in clinical management [6–8]. The HER-2 protein is overexpressed in breast cancer, which is associated with increased invasiveness, higher recurrence rates, and poorer survival outcomes [9, 10]. HER-2 expression has been shown to be not only a significant prognostic factor, but also a vital target for HER-2-directed therapies, enabling more personalized treatment strategies for patients [11]. Currently, the main diagnostic methods for detecting HER-2 tumor cells rely on conventional techniques such as immunohistochemistry (IHC) and flow cytometry [12–14]. However, these methods are limited by issues related to sensitivity and specificity. To address these limitations, the construction of HER-2 targeted bioprobes and the development of highly sensitive detection methods have shown great promise for precise tumor detection [15]. Advancing the development of sensitive and specific diagnostic tools for early breast cancer detection is thus of significant clinical importance, particularly for improving early diagnosis and treatment efficacy [13, 16, 17].

Surface-enhanced Raman spectroscopy (SERS) is an ultra-sensitive analytical technique with broad applications and a promising future [18]. It has been widely used in various fields, including environmental monitoring, food safety, and analytical chemistry [19–24]. It shows the enhancement of Raman signal caused by the interaction of analyte molecules with nanostructured substrates [25]. Electromagnetic mechanism (EM) and chemical mechanism (CM) are attributed to explain most Raman SERS effects. The EM suggests that SERS arises primarily from the localized electromagnetic field enhancement on the surface of metal nanostructures, which significantly amplifies Raman scattering signals [26]. In contrast, the CM emphasizes the chemical interactions between analyte molecules and the substrate surface, such as promoted charge transfer (CT) and changes in molecular polarization, both of which contribute to the enhancement effect [27, 28]. The effectiveness of SERS is highly dependent on the choice of substrate materials. The unique surface plasmon resonance (SPR) effect of noble metal nanoparticles and the photoinduced charge transfer (PICT) phenomenon of semiconductor materials make them promising SERS substrates [29-31]. It is worth noting that noble metals such as gold nanoparticles (Au NPs) have become the mainstream materials for SERS detection due to their superior SERS sensitivity, biocompatibility, controllable morphology, as well as the simplicity and economy of their synthesis methods [32–35].

In recent years, SERS technology has begun to shine in the field of biomedicine. SERS-based cell detection technology has garnered widespread attention, particularly showing great potential in precise tumor detection [36–41]. SERS technology is capable not only of rapidly and efficiently detecting tumor cells but also of non-invasively revealing their fingerprint spectra [42–44]. The detection methods are primarily divided into two categories: label-free SERS detection and labeled SERS detection [45, 46]. The label-free approach involves the direct interaction of SERS bioprobes with analytes, offering good applicability due to its low cost and ease of preparation [47]. However, non-specific binding and significant background noise present major

challenges in precise tumor detection [48, 49]. In contrast, the labeled detection approach employs SERS bioprobes composed of Raman signal molecules and tumor-targeting antibodies, enabling specific binding to the surface of tumor cells [50, 51]. By collecting Raman signals from these bioprobes, tumor cells can be identified, allowing for further accurate localization and imaging of tumor tissues [38, 52]. Therefore, the construction of appropriate SERS bioprobes for labeled detection can effectively, quickly and accurately present information about breast cancer cells and tumor markers, thereby providing valuable guidance for the formulation of treatment plan and prognosis [51, 53].

Since the slight differences in tumor markers expressed by different breast cancer cell types, distinguishing them solely using SERS technology is a huge challenge due to the vast amount of data and high cost in time [54]. Machine learning is an artificial intelligence technique that enables computer systems to automatically learn and improve their performance from experience without explicit programming [55–57]. With its rapid development, machine learning has become indispensable in the field of medical diagnosis due to its efficient ability to data processing, group classification, and predictive analysis [58–62]. Principal Component Analysis (PCA) is one of the most widely used data dimensionality reduction algorithms, which removes noise and unimportant features, thereby enhancing data processing speed [63]. Linear Discriminant Analysis (LDA) is another powerful tool to classify the boundaries between different categories, as well as to make predictions on given datasets [64]. By employing these algorithms, it is possible to analyze complex spectral data, enabling accurate diagnosis, typing, and prognostic prediction in a rapid, reliable and economic way [65, 66]. Thus, with the aid of machine learning, the accuracy and efficiency of SERS technology in detecting tumor cells will be significantly enhanced.

Based on the aforementioned research, this article demonstrates the preparation of two bioprobes, gold nanoparticles Au NPs@4-MBA@PDA@aHER-2 and Au NPs@4-MPY@PDA@aHER-2, for the detection and molecular typing of breast cancer cells with the assistance of machine learning. The Au NPs were synthesized via a one-step method and can detect trace 4-mercaptophenylacetic (4-MBA) and 4-mercaptopyridine (4-MPY) molecules with concentrations as low as 2×10^{-9} M (1 M = 1 mol/L). In addition, the constructed bioprobes exhibited good spectral stability with a relative standard deviation (RSD) of 9.58%. To avoid false positive and improve detection accuracy, two bioprobes and machine learning based data analysis were introduced to distinguish breast cancer cells from white blood cells (WBCs) and to further perform breast cancer cell typing. By building a "symphonic SERS spectra" of the two bioprobes with the PCA-LDA algorithm, the classification accuracy of distinguishing SK-BR-3 cells, MDA-MB-231 cells, and WBCs reached up to 97.33%. These results reveal the potential applications and significant advantages of integrating SERS technology with machine learning classifiers in breast cancer detection and molecular typing.

Experimental Methods

Materials

Chloroauric acid ($HAuCl_4 \cdot 4H_2O$) was purchased from Sinapharm Chemical Reagent Co. Ltd. 4-mercaptophenylacetic acid (4-MBA) and 4-mercaptopyridine (4-MPY) were purchased from Sigma-Aldrich Chemicals Co. Ltd. Sodium citrate ($C_6H_5Na_3O_7$), paraformaldehyde (PFA, 4%), ammonium hydroxide ($NH_3 \cdot H_2O$, 28%), dopamine (DA), and tris-HCl buffer solution (pH = 8.5) were purchased from Aladdin Industrial Corporation in Shanghai, China. Alexa Fluor® 647 Anti-ErbB-2/HER-2 antibody and Anti-ErbB-2 / HER-2 antibody were purchased from Signalway Antibody CCL. Hoechst33342 staining solution was purchased from Beijing Solarbio Biotechnology Co. Ltd.

Preparation of Au NPs

Au NPs were prepared by the citrate reduction method as previously reported in the literature [67, 68]. This method involves adding $HAuCl_4 \cdot 4H_2O$ (5 mL, 5 mmol/L) and sodium citrate solution (5 mL, 1%) to 40 mL of pure water and heating to boiling while stirring. After 10 min, the solution turned purple, and the resulting AuNPs were cooled to room temperature and stored at 4 °C for subsequent experiments.

Synthesis of Au NPs @4-MBA and Au NPs @4-MPY

1 mL of different concentrations of 4-MBA (10^{-8}–

10^{-3} mol/L) and 1 mL of different concentrations of 4-MPY (10^{-8}–10^{-3} mol/L) were added to 5 mL of aforementioned Au NPs solution, respectively, and stirred at 300 r/min for 40 min. The resulting Au NPs@4-MBA and Au NPs@4-MPY were centrifuged at 12 000 r/min for 30 min, dispersed in 5 mL of water, and stored at 4 °C. The SERS intensity was then measured, and samples with the same SERS intensity were selected for further experiments.

Synthesis of Au NPs@4-MBA@PDA@aHER-2 and Au NPs@4-MPY@PDA@aHER-2

1 mL of a 5 mg/mL PDA solution was added to 10 mL of both Au NPs@4-MBA and Au NPs@4-MPY with 4 mL of ethanol. Then, 300 μL of 28% $NH_3 \cdot H_2O$ was added to maintain a pH = 8–10, and the reaction was allowed to proceed for 2 h. Finally, Au NPs@4-MBA@PDA and Au NPs@4-MPY@PDA were centrifuged (12 000 r/min, 30 min) and washed three times, then dispersed in 5 mL of water and stored at 4 °C for subsequent experiments.

HER-2 antibody conjugation: 5 mL of both Au NPs@4-MBA@PDA and Au NPs@4-MPY@PDA were mixed with 5 mL of Tris-HCl buffer (pH = 8.5, 10 mmol/L), centrifuged with tris-HCl buffer (12 000 r/min, 30 min) twice, and then dispersed in 5 mL of tris-HCl buffer. Subsequently, 5 μL of aHER-2 was added to 5 mL of the treated Au NPs@4-MBA@PDA and Au@4-MPY@PDA, and the mixture was oscillated at 200 r/min in the dark for 24 h. Additionally, the final SERS bioprobes were centrifuged three times at 12 000 r/min and dispersed in phosphate buffer (PBS). Similarly, Alexa Fluor 647 (AF 647)-labeled aHER-2 was connected to Au NPs@4-MBA@PDA and Au NPs@4-MPY@PDA to prepare Au NPs@4-MBA@PDA@aHER-2-AF 647 and Au@4-MPY@PDA@aHER-2-AF 647 bioprobes to verify the successful modification of aHER-2 on Au NPs@4-MBA@PDA and Au NPs @4-MPY@ PDA. The prepared bioprobes were stored at 4 °C for subsequent experiments.

Characterization techniques

The morphology and elemental mapping were characterized using high-resolution transmission electron microscopy (HRTEM, Talos F200x, Thermo Fisher Scientific). X-ray diffraction (XRD) analysis was performed using a BRUKER D8 ADVANCE DAVINCI diffractometer equipped with Cu-K_α radiation (λ = 1.540 56 Å). Size distribution and zeta potential measurements were completed by dynamic light scattering (DLS, Malvern, Zetasizer). Ultraviolet–visible (UV–Vis) absorption spectra were tested on a Lambda T10 CS spectrophotometer (PerkinElmer). The concentration of gold in nanoprobes was determined by inductively coupled plasma optical emission spectroscopy (ICP-OES, Spectro Arcos, Spectro). Fluorescence spectra were recorded by a confocal laser scanning microscope (CLSM, TCS SP8, Leica). SERS spectra and images were observed using a confocal Raman microscope (LabRAM Odyssey, Horiba).

Cell culture

Triple-negative breast cancer cell line (MDA-MB-231 cells), human breast normal epithelial cell line (MCF-10A cells), and breast cancer cell line (SK-BR-3 cells) were purchased from Procell Co. Ltd. Cells were cultured under standard conditions (5% CO_2, 37 °C).

In vitro biocompatibility of SERS bioprobes

100 μL of human mammary normal epithelial cell line (MCF-10A cells) (10^5 cells/mL) was added to a 96-well plate and incubated for 24 h. Then, 100 μL of different concentrations (0–80 μg/mL) of Au NPs@4-MBA@PDA@aHER-2 and Au NPs@4-MPY@ PDA@aHER-2 bioprobes were added, after removing the culture medium. The cells were further incubated for 24 h, and cell viability was determined using a CCK-8 assay kit. Each well was added with 10 μL of CCK-8 reagent. After 2 h, the optical density (OD) value at 450 nm was measured using a microplate reader, and cell viability was calculated based on this.

SERS bioprobes cellular uptake assessment

MDA-MB-231 cells and SK-BR-3 cells (10^5 cells/mL, 1 mL) were added to a confocal dish and cultured for 24 h. Then, 1 mL of two bioprobes (10 μg/mL) was added, and the cells were incubated in a CO_2 incubator for 15, 30, and 60 min. After fixation with paraformaldehyde for 15 min, the cells were washed with PBS three times. Subsequently, the cell nuclei were stained with Hoechst33342 (blue), and the cell samples in the confocal dish were detected using CLSM (TCS SP8, Leica) and confocal Raman microscopy.

Isolation of white blood cells from rabbit blood

Rabbit blood was purchased from Nanjing SenBeiJia

Biological Technology Co., Ltd. 2 mL of rabbit blood was mixed with 2 mL of PBS in a centrifuge tube, and peripheral blood lymphocyte separation culture medium (2 mL) was slowly added. After centrifugation at 400× *g* for 25 min, the opalescent cell layer (i.e., WBCs) was collected and washed with PBS three times, then dispersed in 1 mL of PBS.

SERS signal detection of cells

MDA-MB-231 cells, SK-BR-3 cells, and WBCs (each 10^5 cells/mL) were resuspended and incubated with 1 mL of 10 μg/mL Au NPs@4-MBA@PDA@aHER-2 and 1 mL of 20 μg/mL Au NPs@4-MPY@PDA@aHER-2, respectively, in a 5%CO_2 incubator at 37 °C for 30 min. The cells were centrifuged and washed three times, then dispersed in 20 μL of PBS solution. The final cells were placed on a glass slide and analyzed using confocal Raman microscopy. Each type of cell was fixed on a silicon wafer, and 50 cells of each type were randomly selected.

Raman spectra data processing and statistical analysis

A total of fifty SERS spectra from each cell line were analyzed, covering the spectral range from 800 to 1 800 cm^{-1}. The Raman spectral data underwent a series of preprocessing steps, including baseline correction, signal smoothing, and normalization. The Whittaker algorithm was utilized for signal smoothing, while the arPLS algorithm was employed for baseline correction. The preprocessing of the data was performed using Python version 3.7 in conjunction with the RamPy package. The dataset, comprising 50 spectra, underwent analysis through principal component analysis (PCA) and linear discriminant analysis (LDA) algorithms. PCA, which is an unsupervised technique, was applied to facilitate dimensionality reduction of the data, whereas LDA was employed for the classification of the processed data. To mitigate the risk of overfitting, K-fold cross-validation was utilized. Furthermore, the receiver operating characteristic (ROC) curve was constructed to evaluate model's performance.

Results and Discussion

Preparation and characterization of SERS substrates and bioprobes

Au NPs are one of the preferred SERS materials for analysis, as they can significantly enhance the Raman scattering signal of analytes [67, 69, 70]. The synthesis of SERS bioprobes is illustrated in Scheme 1. As shown in Fig. 1(a), the synthesized Au NPs exhibited near-circular structures with an average diameter of approximately 20 nm. The high-resolution transmission electron microscopy (HRTEM) was utilized to perform lattice fringes and selected area electron diffraction (SAED) of Au NPs as depicted in Figs. 1(b) and 1(c). Clear lattice planes were observed, with the measured lattice fringe spacing being 0.235 5 nm, demonstrating a (1, 1, 1) lattice orientation [71, 72]. The SAED patterns also confirmed the stable crystal structure of Au NPs with stable crystal structure. The elemental distribution was analyzed through energy-dispersive X-ray spectroscopy (EDS) mapping, as shown in Figs. 1(d)–1(f), which further validated the successful synthesis of Au NPs. Moreover, the crystallographic property of Au NPs was characterized using X-ray powder diffraction (XRD, Fig. 1(g)). To build reliable SERS bioprobes, polydopamine (PDA) was used for enhancing the soluble stability and providing conjugation site for aHER-2 [51]. As shown in Fig. 1(h), the PDA layer was coated on the outer layer of the Au NPs. The conjugation of aHER-2 on the Au NPs@PDA surface was confirmed by the appearance of N-H stretching vibrations at 1 510–1 570 cm^{-1}, as well as the characteristic CO-NH vibrations at 1 200–1 350 cm^{-1} in the infrared spectra. Additionally, as shown in Fig. S1 in the Electronic Supplementary Material (ESM), the sizes of Au NPs, Au NPs@4-MBA@PDA, and Au NPs@4-MPY@PDA were analyzed by dynamic light scattering (DLS), with the hydrodynamic diameter of the nanoparticles being roughly consistent with their HRTEM results. Due to the modification with PDA and aHER-2, the hydrodynamic size of the Au NPs@4-MBA (4-mercaptobenzoic acid) and Au NPs@4-MPY (4-mercaptopyridine) increased, with corresponding changes observed in the surface potentials of the nanoparticles, as shown in Fig. S2 in the ESM. Furthermore, Fig. S3 in ESM presents the UV–Vis

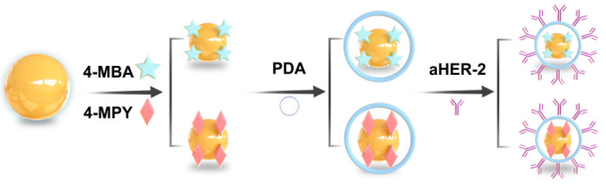

Scheme 1 The synthesis of SERS bioprobes.

spectra of the nanoparticles during the synthesis process, with changes in the absorption peaks after modification with PDA and aHER-2. The above results demonstrate the successful fabrication of Au NPs and the construction of bioprobes.

The characterization of the SERS performance of the bioprobes

In order to evaluate the SERS performance of Au NPs, the SERS spectra of Au NPs@4-MBA, and Au NPs@4-MPY under 633 nm excitation were obtained. As shown in Figs. 2(a) and 2(b), multiple characteristic Raman peaks of 4-MBA and 4-MPY molecules were observed. When the concentrations of these signal molecules were reduced to 2×10^{-9} mol/L, the vibrational peaks remained resolvable, indicating that the limit of detection (LOD) for 4-MBA and 4-MPY molecules on Au NPs can be achieved at 2×10^{-9} mol/L. Figs. S4 and S5 in the ESM illustrate the heatmap and spectral repeatability of Au NPs@4-MBA. The RSD values at the peak positions of 1 080 and 1 588 cm^{-1} were 7.68% and 6.47%, respectively. Similarly, Figs. S6 and S7 in the ESM depict the spectral repeatability of Au NPs@4-MPY, with the RSD values of 8.90% and 17.99% at the 1 094 and 1 610 cm^{-1}, respectively. These results indicated that both Au NPs@4-MBA and Au NPs@4-MPY exhibited good spectral stability. During the probe construction process, concentrations of 2×10^{-6} mol/L for 4-MBA and 4-MPY molecules were selected for subsequent experiments due to their similar signal intensities. Following encapsulation with PDA, a significant reduction in the SERS signal was observed, which can be attributed to the shielding

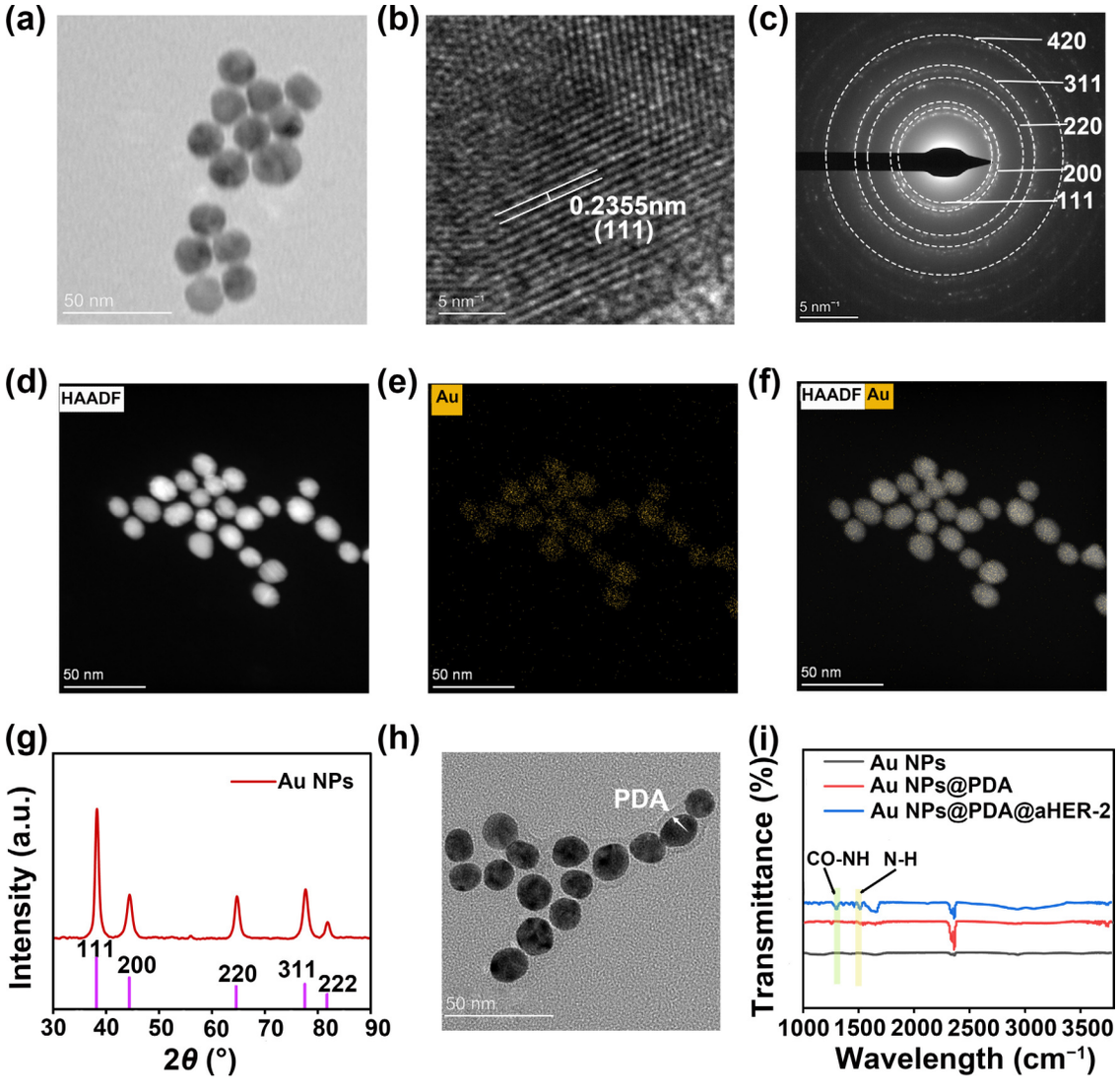

Fig. 1 Morphology characterization of bioprobes. **(a)** TEM image, **(b)** lattice fringe, **(c)** SAED image, **(d–f)** HRTEM mapping and **(g)** XRD spectrum of Au NPs, **(h)** HRTEM image of Au NPs@PDA, **(i)** Infrared spectra of Au NPs, Au NPs@PDA, and Au NPs@PDA@aHER-2.

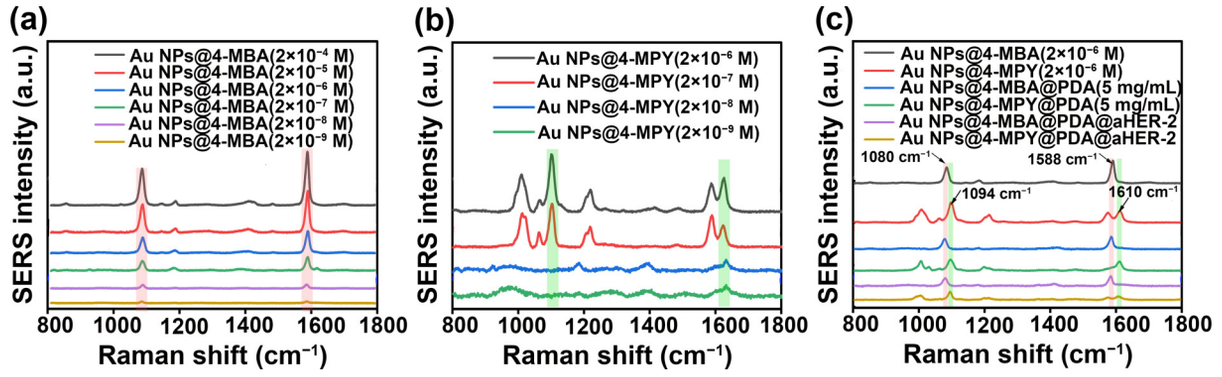

Fig. 2 SERS performance of two bioprobes. **(a)** SERS spectra of Au NPs@4-MBA (LOD = 2 × 10^{-9} mol/L), **(b)** SERS spectra of Au NPs@4-MPY(LOD = 2 × 10^{-9} mol/L), and **(c)** SERS spectra of AuNPs, Au NPs@4-MBA@PDA(4-MBA: 2 × 10^{-6} mol/L, PDA: 5 mg/mL), Au NPs@4-MBA@PDA@aHER-2, Au NPs@4-MPY@PDA(4-MPY: 2×10^{-6} mol/L, PDA: 5 mg/mL), Au NPs@4-MPY@PDA@aHER-2.

effect of the macromolecular layer. Nevertheless, the signal intensity exhibited only a slight decrease after the conjugation with aHER2 antibodies, highlighting the detection potential of the SERS bioprobes (Fig. 2(c)).

To assess the SERS stability of Au NPs@4-MBA@PDA@aHER-2, Fig. 3(a) and 3(b) demonstrate the intensity heatmap and 10 points of SERS spectra of Au NPs@4-MBA@PDA@aHER-2. Figs. 3(c) and 3(d) show that the RSD values at the 1 080 and 1 588 cm^{-1} peak positions for Au NPs@4-MBA@PDA@ aHER-2 were 9.84% and 10.68%, respectively. These findings suggested that Au NPs@4-MBA@PDA@ aHER-2 bioprobe possessed good stability.

To appraise the SERS stability of Au NPs@4-

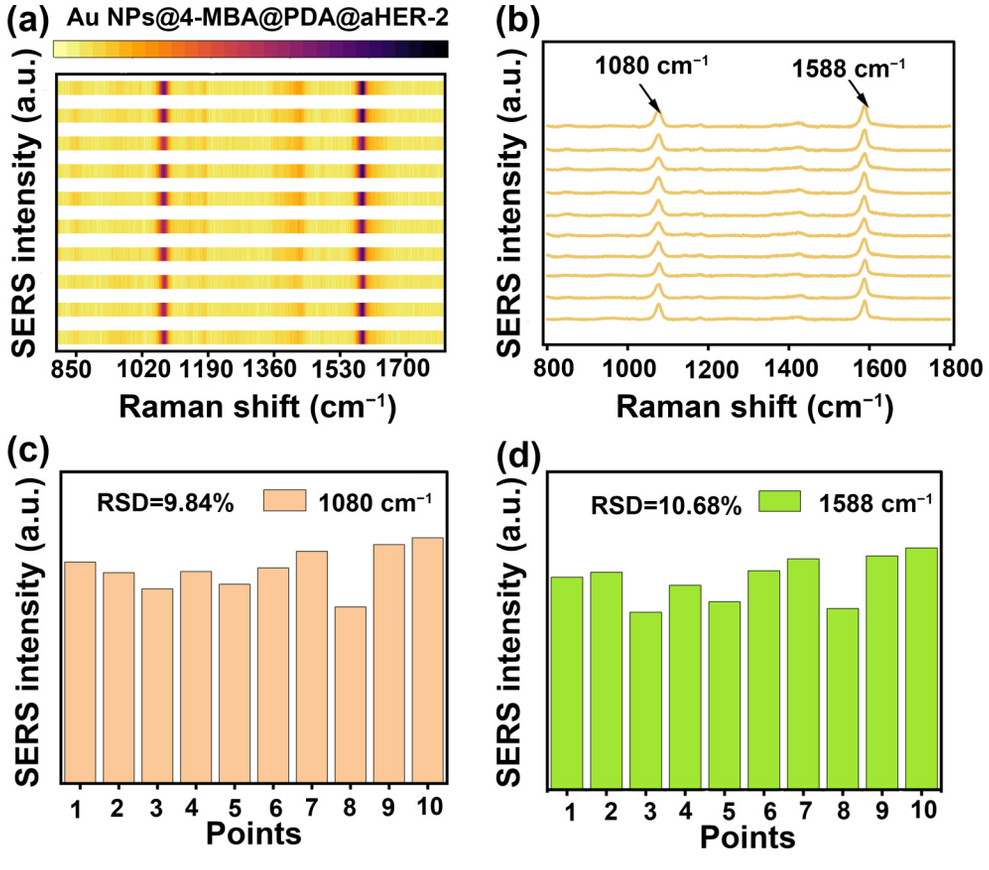

Fig. 3 SERS spectral repeatability of Au NPs@4-MBA@PDA@aHER-2 (4-MBA: 2 × 10^{-6} mol/L, PDA: 5 mg/mL). **(a)** Intensity heatmap and **(b)** 10 points of SERS spectra of Au NPs@4-MBA@PDA@aHER-2, specific peak signal stability at **(c)** 1 080 cm^{-1} and **(d)** 1 588 cm^{-1} of Au NPs@4-MBA.

MPY@PDA@aHER-2, Figs. 4(a) and 4(b) present the intensity heatmap and 10 points of SERS spectra of Au NPs@4-MPY@PDA@aHER-2. Figs. 4(c) and 4(d) illustrate that the RSD values at the 1 094 and 1 610 cm^{-1} peaks of Au NPs@4-MPY@PDA@aHER-2 are 9.58% and 10.28%, respectively. These results indicated that Au NPs@4-MPY@PDA@aHER-2 exhibited good stability.

The targeting effect and specificity of SERS bioprobes

Differentiating HER2-positive SK-BR-3 cells from triple-negative MDA-MB-231 cells is crucial for the development of precise treatment. Individuals with HER2-positive breast cancer might need targeted HER-2 therapies, while patients with TNBC might require chemotherapy or immunotherapy. To confirm whether targeting aHER-2 was successfully conjugated to the bioprobes, fluorescent Alexa Fluor 647 (AF 647) labeled aHER-2 was used to yield Au NPs@4-MBA@PDA@aHER-2-AF 647 and Au NPs@4-MPY@PDA@aHER-2-AF 647. Under confocal laser scanning microscopy (CLSM), the bright-field and fluorescence images of both bioprobes were completely overlapped and matched (Fig. S8 in the ESM), confirming the effective linkage of aHER-2 to Au NPs. Subsequently, MDA-MB-231 cells and SK-BR-3 cells were co-incubated with Au NPs@4-MBA@PDA@aHER-2-AF 647 and Au NPs@4-MPY@PDA@aHER-2-AF 647 for 15 min, 30 min, and 60 min to evaluate their targeting effects. As shown in Fig. 5(a), both SERS bioprobes were adhered to SK-BR-3 cells, indicating that they were endowed with good targeting ability. However, due to the non-specific adsorption of the probe on the cell surface, MDA-MB-231 cells will also bind to the probes (Fig. 5(b)). To further distinguish the targeting specificity of SERS bioprobes for the two subtypes of breast cells, the fluorescence intensity of the HER-2 antibody was quantified. As shown by the average gray value in Fig. S9 in the ESM, more bioprobes adhered to SK-BR-3 cells than to MDA-MB-231 cells, indicating that both SERS bioprobes showed targeting capabilities with a high degree of specificity towards SK-BR-3 cells. In addition, an incubation time of 30 min was chosen for subsequent

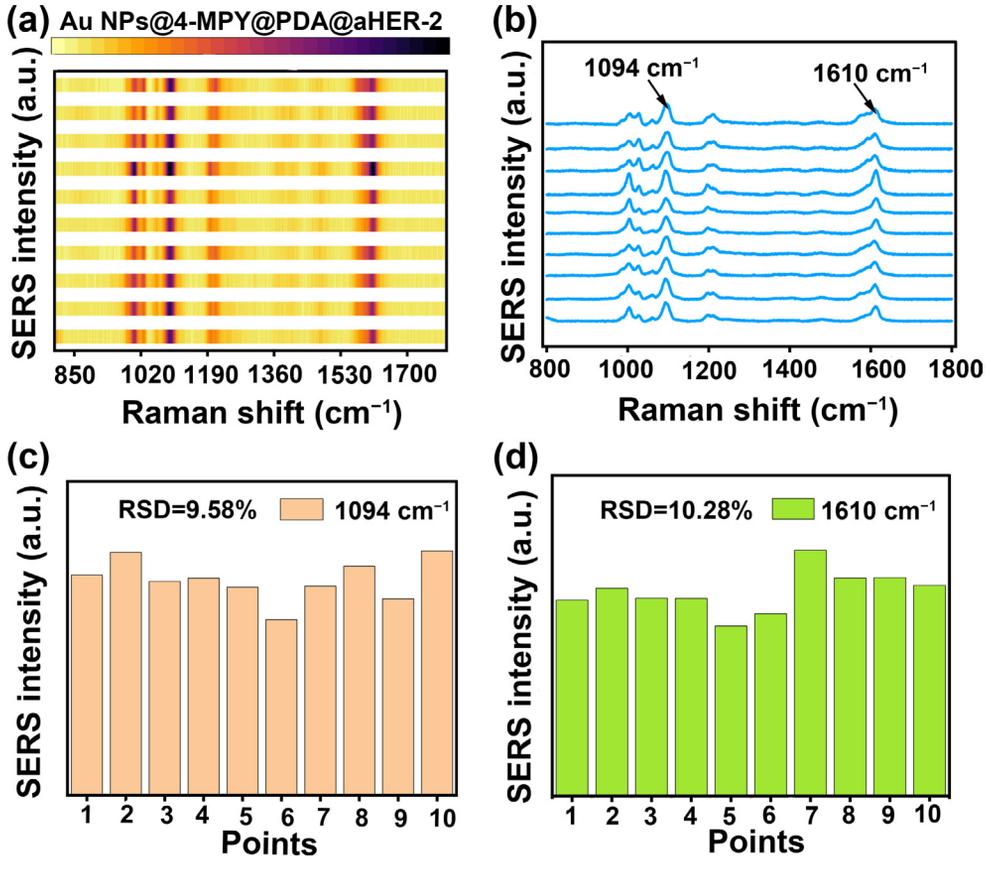

Fig. 4 SERS spectral repeatability of Au NPs@4-MPY@PDA@aHER-2 (4-MPY: 2×10^{-6} mol/L, PDA: 5 mg/mL). **(a)** Intensity heatmap and **(b)** 10 points of SERS spectra of Au NPs@4-MPY@PDA@aHER-2, specific peak signal stability at **(c)** 1 094 cm^{-1} and **(d)** 1 610 cm^{-1} of Au NPs@4-MBA.

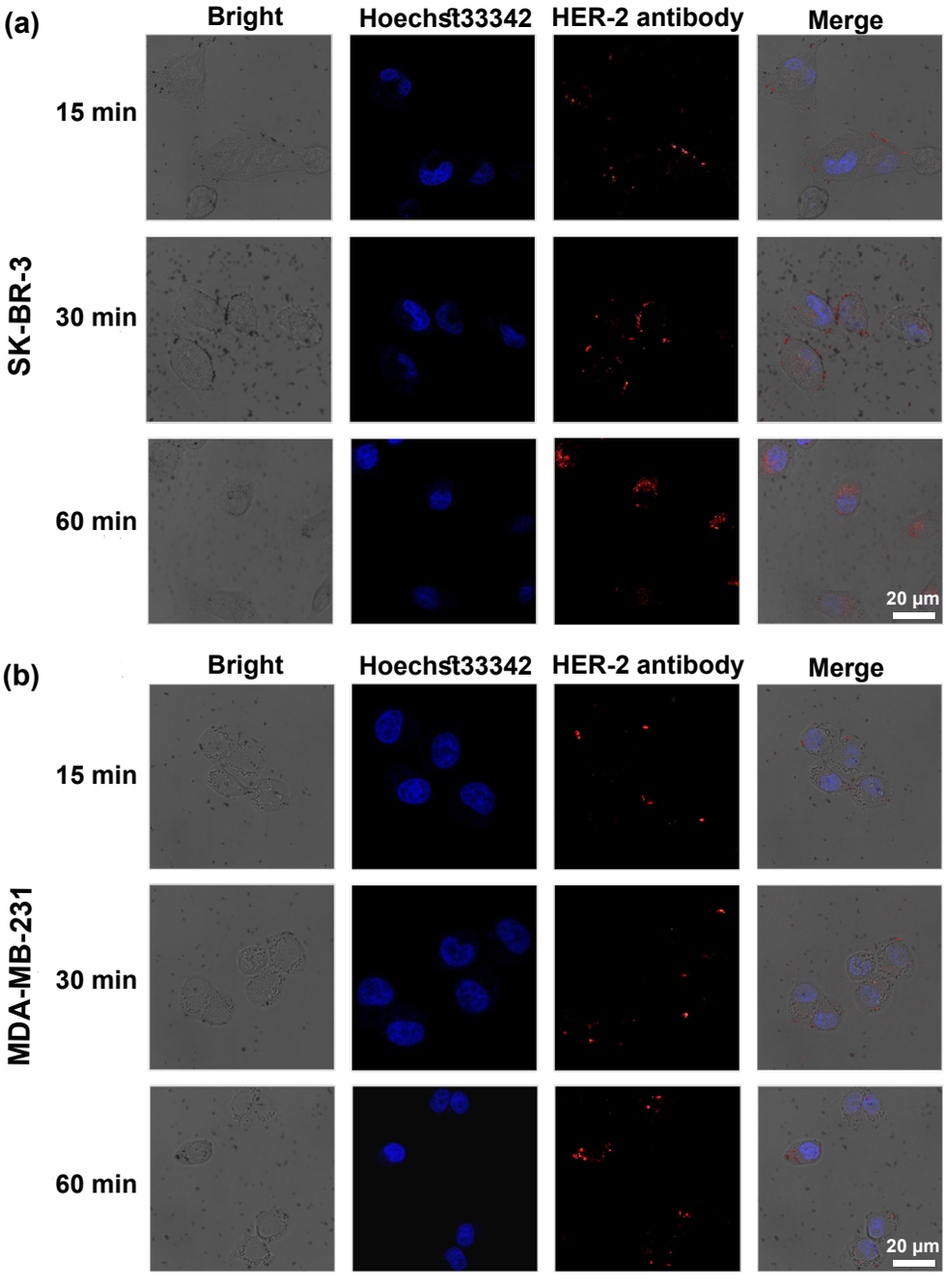

Fig. 5 Fluorescence imaging was conducted on **(a)** SK-BR-3 cells and **(b)** MDA-MB-231 cells incubated with Au NPs@4-MBA@PDA@aHER-2 and Au NPs@4-MPY@PDA@aHER-2 for varying time intervals.

experimental condition, because obvious targeting results could be obtained. There was no statistical significance in the incubation results of 15 min, likely due to the insufficient time for effective binding. Furthermore, the cytotoxicity of the two SERS bioprobes was tested using the CCK-8 assay. The results showed (Fig. S10 in the ESM) a cell survival rate above 80%, suggesting good biocompatibility of the constructed SERS bioprobes.

Before the statistical analysis of cell classification, the optimal concentration for SERS bioprobes incubated with cells was explored. Au NPs@4-MBA@PDA@aHER-2 and Au NPs@4-MPY@PDA@aHER-2 at concentrations of 5, 10, and 20 mg/L were incubated with SK-BR-3 cells for 30 min. The SERS spectra of the bioprobes and cells were recorded under 633 nm excitation. After preprocessing the spectra, we have obtained the average signal intensity at the 1 080 and 1 094 cm^{-1} peak positions, as shown in Fig. S11 in the ESM. Ultimately, 1 mL of 10 μg/mL Au NPs@4-MBA@PDA@aHER-2 and 1 mL of 20 μg/mL Au NPs@4-MPY@PDA@aHER-2 were used. The

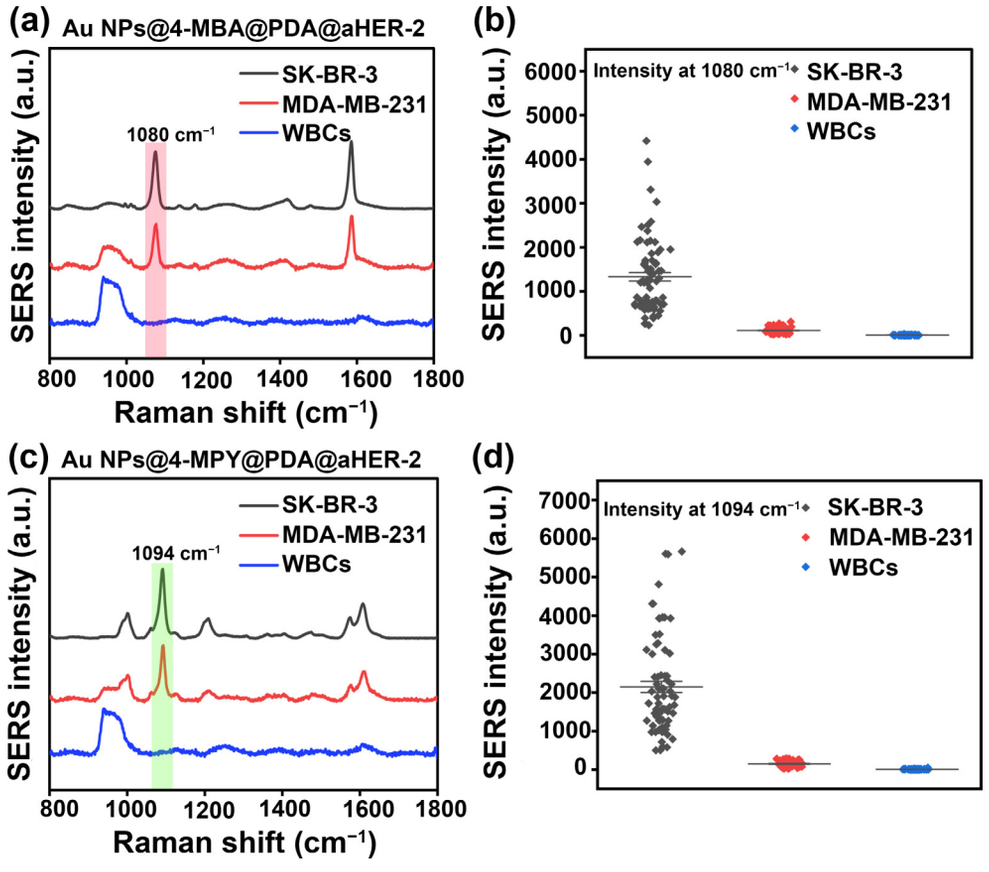

Fig. 6 The average SERS spectra and the main characteristic Raman peaks of SK-BR-3 cells, MDA-MB-231 cells, and WBCs were recorded using a 633 nm excitation source. **(a)** The average SERS spectrum of 4-MBA, **(b)** the intensity at 1 080 cm^{-1}, **(c)** the average SERS spectrum of 4-MPY, and **(d)** the intensity at 1 094 cm^{-1}. The Raman testing conditions for the SERS spectra were as follows: laser wavelength: 633 nm; laser power: 25%; lens: 50× objective; time: 5 s.

Raman spectra, when excited at a wavelength of 633 nm, successfully detected the 4-MBA and 4-MPY molecules present in the bioprobes. MDA-MB-231 cells also presented significant intensity, while WBCs showed the weakest intensity. This characteristic was further confirmed by calculating the intensity at 1 080 cm^{-1} peak (corresponding to 4-MBA) as depicted in Fig. 6(b). Similarly, calculating the intensity at the 1 094 cm^{-1} peak (corresponding to 4-MPY) yielded the same results, as shown in Fig. 6(d).

Machine learning application in breast cancer diagnosis and molecular subtyping

In this study, SERS bioprobes were integrated with machine learning algorithms to analyze and classify the comprehensive SERS data for the diagnosis of breast cancer. In practical conditions, it is essential to identify and distinguish WBCs, one of the main components of a blood sample, avoiding the false positive results in tumor cells detection. WBCs were also involved in the classification model to realize the differentiation of various cell types.

To classify two breast cancer cell subtypes and WBCs, fifty SERS spectra from each cell line were collected. These SERS data were then processed using PCA for dimensionality reduction and LDA for clustering analysis with a training-to-test set ratio of 7:3. The average SERS spectra of the single bioprobe and dual bioprobes enabled "symphonic SERS spectra" were illustrated in Fig. 7(a). It was found that the 5-fold cross-validation accuracy of the Au NPs@4-MBA@PDA@aHER-2 bioprobe in distinguishing SK-BR-3 cells, MDA-MB-231 cells, and WBCs was only 86.24%. The Au NPs@4-MPY@PDA@aHER-2 bioprobe in distinguishing the same cell types was 84.46%. In contrast, the classification accuracy after building "symphonic SERS spectra" remarkably increased to 97.33% (Fig. 7(b)). The 2D LDA score plot for SK-BR-3 cells, MDA-MB-231 cells, and WBCs, which was calculated based on the results of PCA dimensionality reduction (Fig. S12 in ESM), was depicted in Fig. 7(c). It can be seen that three types of cells were clearly classified and separated in the LDA space. In addition, each cell type's sample points were enclosed by confidence ellipses,

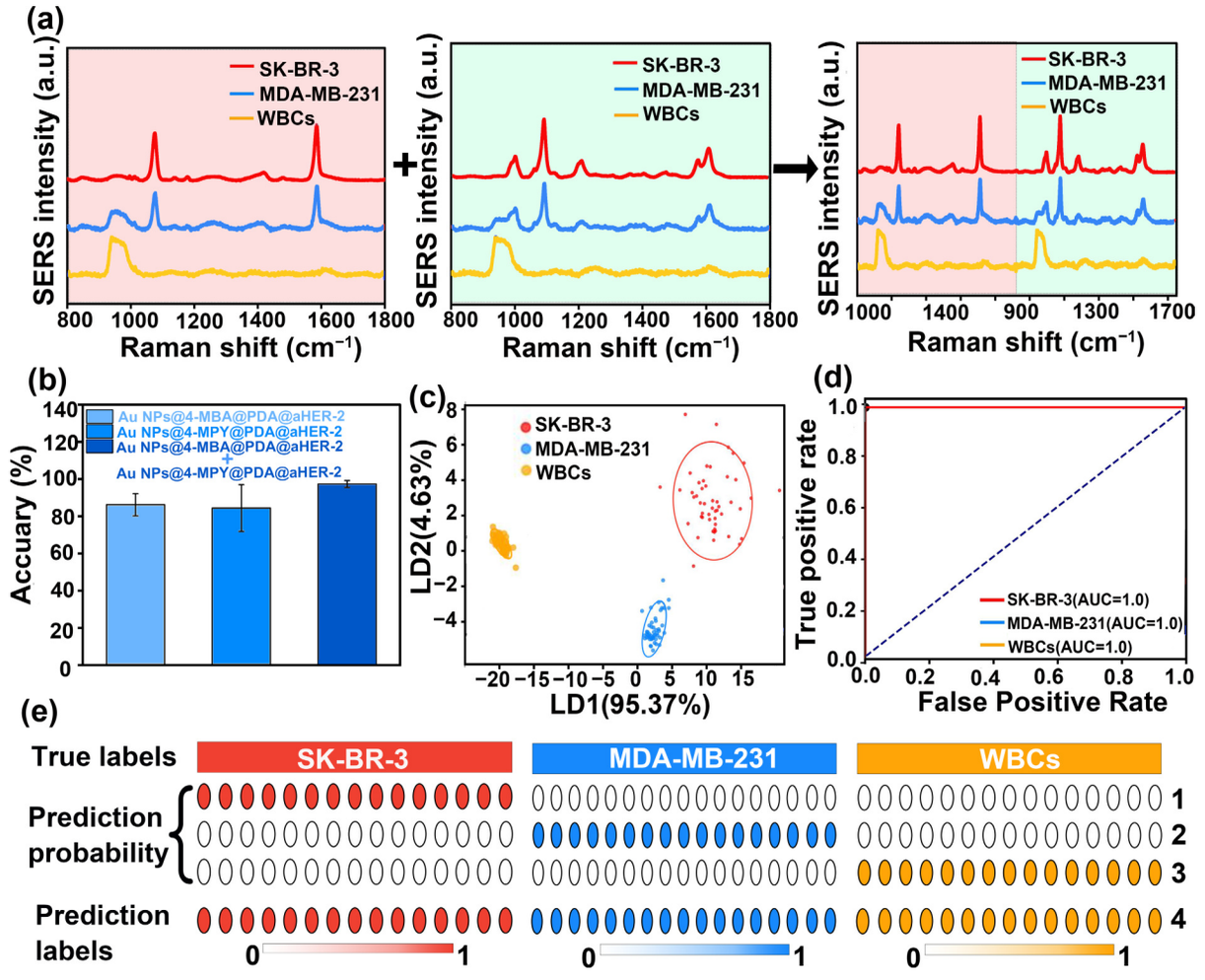

Fig. 7 The result of machine learning analysis. **(a)** The integration of two bioprobes' SERS spectra, **(b)** the classification accuracy of Au NPs@4-MBA@PDA@aHER-2, Au NPs@4-MPY@PDA@aHER-2, and the combined Au NPs@4-MBA@PDA@aHER-2 with Au NPs@4-MPY@PDA@aHER-2 in differentiating between SK-BR-3 cells, MDA-MB-231 cells, and WBCs, **(c)** a 2D LDA score plot for SK-BR-3 cells, MDA-MB-231 cells, and WBCs, **(d)** the ROC curve derived from the validation set results of the PCA-LDA model, and **(e)** the scores of the validation set as predicted by the trained PCA-LDA model.

indicating that the data points of each class were relatively concentrated.

The classification model was further assessed by plotting ROC curves, which can provide a graphical representation of the trade-off between sensitivity (true positive rate) and 1-specificity (false positive rate). The area under the curve (AUC) of the ROC is a crucial metric for evaluating model performance. When the AUC value approaches 1.0, it demonstrates that the model has approximately perfect discrimination ability. In the ROC curve for distinguishing three types of cells using "symphonic SERS spectra", the AUC values were all 1.0, indicating the high efficiency and reliability of the classification model (Fig. 7(d)). The specific classification results for the test set are listed in Table S1 in the ESM and Fig. 7(e) graphically displays the model's predicted results for the three types of cells with color coding representing the prediction probabilities. The middle rows 1–3 show the model's predicted probabilities for each cell by ellipses. The darker elliptical shape indicates a higher probability of correct prediction, with the probability approaching 100%. The 4th row represents the model's final prediction results, showing that all prediction results are entirely accurate. These results demonstrated that all samples within the test set were predicted with precision, and the PCA-LDA model displayed a high degree of reliability in differentiating between HER-2$^+$ and HER-2$^-$ breast cancer cell lines.

Conclusions

In summary, this study presents the development of two SERS-based bioprobes, Au NPs@4-

MBA@PDA@aHER-2 and Au NPs@4-MPY@PDA@aHER-2, for the detection and molecular typing of breast cancer cells. The synthesized Au NPs exhibited high uniformity, enabling the detection of trace amounts of 4-MBA and 4-MPY molecules at concentrations as low as 2×10^{-9} mol/L. The bioprobes also demonstrated excellent spectral stability, with RSD of 9.58%. To minimize false positives and improve detection precision, two bioprobes approach coupled with machine learning-based data analysis was employed to differentiate breast cancer cells from WBCs. Utilizing a "symphonic SERS spectra" analysis combined with the PCA-LDA algorithm, the classification accuracy for distinguishing SK-BR-3 cells, MDA-MB-231 cells, and WBCs achieved a high of 97.33%. These findings underscore the promising applications and significant advantages of integrating SERS technology with machine learning classifiers in the field of breast cancer detection and molecular typing.

CRediT Author Statement

Xinyu Miao, Yujiao Xie, Lei Xu, and Li Sun: visualization, writing original draft, writing–review, and editing. **Jiahao Zhang, Xiawei Xu, and Yue Hu:** validation, resources, and investigation. **Zhouxu Zhang, Aochi Liu, and Zhiwei Hou:** data curation, formal analysis, and investigation. **Aiguo Wu and Jie Lin:** conceptualization, methodology, project administration, and supervision.

Acknowledgements

We acknowledge the supporting from the National Science and Technology Major Project (No. 2023ZD0500902), National Natural Science Foundation of China (Nos. 32311530040, 12374390, 32025021, and 31971292), the member of Youth Innovation Promotion Association Foundation of CAS, China (No. 2023310), and the Key Scientific and Technological Special Project of Ningbo City (No. 2023Z209), Ningbo Youth Science and Technology Innovation Leading Talents Project (No. 2024QL029).

Conflict of Interests

The authors declare no conflict of interest.

Supporting Information

Supporting information to this article can be found online at https://doi.org/10.26599/NBE.2025.9290113.

References

[1] B. Han, R. Zheng, H. Zeng, et al. Cancer incidence and mortality in China, 2022. *Journal of the National Cancer Center*, 2010, 4: 47−53. https://doi.org/10.1016/j.jncc.2024.01.006

[2] A.N. Giaquinto, H. Sung, K.D. Miller, et al. Breast cancer statistics, 2022. *CA: A Cancer Journal for Clinicians*, 2022, 72(6): 524−541. https://doi.org/10.3322/caac.21754

[3] Z.Y. He, Z. Chen, M.D. Tan, et al. A review on methods for diagnosis of breast cancer cells and tissues. *Cell Proliferation*, 2020, 53(7): e12822. https://doi.org/10.1111/cpr.12822

[4] P.A. Carney, J.P. Yi, L.A. Abraham, et al. Reactions to uncertainty and the accuracy of diagnostic mammography. *Journal of General Internal Medicine*, 2007, 22(2): 234−241. https://doi.org/10.1007/s11606-006-0036-9

[5] D. Barba, A. León-Sosa, P. Lugo, et al. Breast cancer, screening and diagnostic tools: All you need to know. *Critical Reviews in Oncology/Hematology*, 2021, 157: 103174. https://doi.org/10.1016/j.critrevonc.2020.103174

[6] Y. Bareche, D. Venet, M. Ignatiadis, et al. Unravelling triple-negative breast cancer molecular heterogeneity using an integrative multiomic analysis. *Annals of Oncology*, 2018, 29(4): 895−902. https://doi.org/10.1093/annonc/mdy024

[7] A. Li, J.M. Keck, S. Parmar, et al. Characterizing advanced breast cancer heterogeneity and treatment resistance through serial biopsies and comprehensive analytics. *NPJ Precision Oncology*, 2021, 5: 28. https://doi.org/10.1038/s41698-021-00165-4

[8] M.A. Subhan, F. Parveen, H. Shah, et al. Recent advances with precision medicine treatment for breast cancer including triple-negative sub-type. *Cancers*, 2023, 15(8): 2204. https://doi.org/10.3390/cancers15082204

[9] N. Iqbal, N. Iqbal. Human epidermal growth factor receptor 2 (HER2) in cancers: Overexpression and therapeutic implications. *Molecular Biology International*, 2014, 2014: 852748. https://doi.org/10.1155/2014/852748

[10] P. Tarantino, D. Trapani, G. Curigliano. Mastering the use of novel anti-HER2 treatment options. *JCO Oncology Practice*, 2021, 17(10): 605−606. https://doi.org/10.1200/OP.21.00216

[11] J.S. Ross, J.A. Fletcher, G.P. Linette, et al. The HER-2/*neu* gene and protein in breast cancer 2003: Biomarker and target of therapy. *The Oncologist*, 2003, 8(4): 307−325. https://doi.org/10.1634/theoncologist.8-4-307

[12] C. Gutierrez, R. Schiff. HER2: Biology, detection, and clinical implications. *Archives of Pathology & Laboratory Medicine*, 2011, 135(1): 55−62. https://doi.org/10.5858/2010-0454-rar.1

[13] A. Aisa, S.S. Weng, X.Y. Li, et al. Immune checkpoint inhibitors combined with HER-2 targeted therapy in HER-2 positive gastroesophageal cancer. *Critical Reviews in Oncology/Hematology*, 2022, 180: 103864. https://doi.org/10.1016/j.critrevonc.2022.103864

[14] Y. Xu, C.J. Wang, Y.L. Xu, et al. Changes in the detection of human epidermal growth factor receptor 2 gene (Her-2) status for Her-2 fluorescent *in situ*

hybridization testing. *Chinese Medical Journal*, 2022, 135(7): 849−850. https://doi.org/10.1097/cm9.0000000000001733

[15] M. Yarbakht, M. Nikkhah, A. Moshaii, et al. Simultaneous isolation and detection of single breast cancer cells using surface-enhanced Raman spectroscopy. *Talanta*, 2018, 186: 44−52. https://doi.org/10.1016/j.talanta.2018.04.009

[16] S.M. Swain, M. Shastry, E. Hamilton. Targeting HER2-positive breast cancer: Advances and future directions. *Nature Reviews Drug Discovery*, 2023, 22(2): 101−126. https://doi.org/10.1038/s41573-022-00579-0

[17] M. Kumar, U. Kumar, A.K. Singh. Therapeutic nanoparticles: Recent developments and their targeted delivery applications. *Nano Biomedicine and Engineering*, 2022, 14(1): 38−52. https://doi.org/10.5101/nbe.v14i1.p38-52

[18] C.Y. Meng, Z. Chen, G. Li, et al. Nanoplatforms for mRNA therapeutics. *Advanced Therapeutics*, 2021, 4(1): 2000099. https://doi.org/10.1002/adtp.202000099

[19] J.Y. Cao, S. Hu, W.X. Tang, et al. Reactive hydrogel patch for SERS detection of environmental formaldehyde. *ACS Sensors*, 2023, 8(5): 1929−1938. https://doi.org/10.1021/acssensors.2c02676

[20] H. Kim, B.T. Trinh, K.H. Kim, et al. Au@ZIF-8 SERS paper for food spoilage detection. *Biosensors & Bioelectronics*, 2021, 179: 113063. https://doi.org/10.1016/j.bios.2021.113063

[21] X.M. Tang, H. Jiang, R.M. Wen, et al. Advancements and challenges on SERS-based multimodal biosensors for biotoxin detection. *Trends in Food Science & Technology*, 2024, 152: 104672. https://doi.org/10.1016/j.tifs.2024.104672

[22] L. Guerrini, R.A. Alvarez-Puebla. Multiplex SERS chemosensing of metal ions *via* DNA-mediated recognition. *Analytical Chemistry*, 2019, 91(18): 11778−11784. https://doi.org/10.1021/acs.analchem.9b02385

[23] X.Y. Meng, J. Yu, W.X. Shi, et al. SERS detection of trace carcinogenic aromatic amines based on amorphous MoO_3 monolayers. *Angewandte Chemie International Edition*, 2024, 63(33): e202407597. https://doi.org/10.1002/anie.202407597

[24] J.L. Jiang, X.Y. Cui, Y.X. Huang, et al. Advances and prospects in integrated nano-oncology. *Nano Biomedicine and Engineering*, 2024, 16(2): 152−187. https://doi.org/10.26599/nbe.2024.9290060

[25] S. Schlücker. Surface-enhanced Raman spectroscopy: Concepts and chemical applications. *Angewandte Chemie International Edition*, 2014, 53(19): 4756−4795. https://doi.org/10.1002/anie.201205748

[26] Q.Q. Li, H.Q. Huo, Y. Wu, et al. Design and synthesis of SERS materials for *in vivo* molecular imaging and biosensing. *Advanced Science*, 2023, 10(8): e2202051. https://doi.org/10.1002/advs.202202051

[27] M.L. Patterson, M.J. Weaver. Surface-enhanced Raman spectroscopy as a probe of adsorbate-surface bonding: Simple alkenes and alkynes adsorbed at gold electrodes. *The Journal of Physical Chemistry*, 1985, 89(23): 5046−5051. https://doi.org/10.1021/j100269a032

[28] M.J. Zhang, X.Y. Meng, J. Yu, et al. A novel Fe_2O_3@CeO_2 heterojunction substrate with high surface-enhanced Raman scattering performance. *SmartMat*, 2024, 5(6): e1301. https://doi.org/10.1002/smm2.1301

[29] X.T. Wang, L. Guo. SERS activity of semiconductors: Crystalline and amorphous nanomaterials. *Angewandte Chemie International Edition*, 2020, 59(11): 4231−4239. https://doi.org/10.1002/anie.201913375

[30] O. Guselnikova, H. Lim, H.J. Kim, et al. New trends in nanoarchitectured SERS substrates: Nanospaces, 2D materials, and organic heterostructures. *Small*, 2022, 18(25): e2107182. https://doi.org/10.1002/smll.202107182

[31] J. Lin, J. Yu, O.U. Akakuru, et al. Low temperature-boosted high efficiency photo-induced charge transfer for remarkable SERS activity of ZnO nanosheets. *Chemical Science*, 2020, 11(35): 9414−9420. https://doi.org/10.1039/d0sc02712j

[32] J. Yu, C. Chen, J. Lin, et al. Amorphous $Co(OH)_2$ nanocages achieving efficient photo-induced charge transfer for significant SERS activity. *Journal of Materials Chemistry C*, 2022, 10(5): 1632−1637. https://doi.org/10.1039/d1tc05770g

[33] G. Awiaz, J. Lin, A.G. Wu. Recent advances of Au@Ag core–shell SERS-based biosensors. *Exploration*, 2023, 3(1): 20220072. https://doi.org/10.1002/EXP.20220072

[34] N. Sher, M. Ahmed, N. Mushtaq, et al. Acetylcholinesterase activity in the brain of rats: Presence of an inhibitor of enzymatic activity in *Heliotropium eichwaldi* L. induced silver/gold allied bimetallic nanoparticles. *Nano Biomedicine and Engineering*, 2023, 15(3): 317−329. https://doi.org/10.26599/nbe.2023.9290034

[35] A. Shekhar, S. Singh, K. Gupta, et al. Comprehensive review of available nanotechnological techniques for treating nonsolid tumors. *Nano Biomedicine and Engineering*, 2023, 15(2): 191−198. https://doi.org/10.26599/nbe.2023.9290023

[36] H.Q. Liu, X. Gao, C. Xu, et al. SERS tags for biomedical detection and bioimaging. *Theranostics*, 12(4): 1870–1903. https://doi.org/10.7150/thno.66859

[37] X.Y. Meng, L. Qiu, G.C. Xi, et al. Smart design of high-performance surface-enhanced Raman scattering substrates. *SmartMat*, 2021, 2(4): 466−487. https://doi.org/10.1002/smm2.1058

[38] J. Lin, X.H. Ma, A.R. Li, et al. Multiple valence states of Fe boosting SERS activity of Fe_3O_4 nanoparticles and enabling effective SERS-MRI bimodal cancer imaging. *Fundamental Research*, 2024, 4(4): 858−867. https://doi.org/10.1016/j.fmre.2022.04.018

[39] M. He, J. Lin, O.U. Akakuru, et al. Octahedral silver oxide nanoparticles enabling remarkable SERS activity for detecting circulating tumor cells. *Science China Life Sciences*, 2022, 65(3): 561−571. https://doi.org/10.1007/s11427-020-1931-9

[40] Y.M. Zhang, L. Lin, J. Ye. A rapid and universal method for depth estimation of lesions in heterogeneous tissues *via* photosafe ratiometric transmission Raman spectroscopy. *View*, 2023, 4(4): 20230022. https://doi.org/10.1002/viw.20230022

[41] X. Zhao, X.J. Liu, D.X. Chen, et al. Plasmonic trimers designed as SERS-active chemical traps for subtyping of lung tumors. *Nature Communications*, 2024, 15: 5855. https://doi.org/10.1038/s41467-024-50321-0

[42] L. Xu, Y.J. Xie, J. Lin, et al. Advancements in SERS-based biological detection and its application and perspectives in pancreatic cancer. *ESS Open Archive Eprints*, 2023, 553: 55324580. https://doi.org/10.22541/au.169199835.55324580/v1

[43] X.W. Xu, J. Lin, Y.H. Guo, et al. TiO_2-based Surface-Enhanced Raman Scattering bio-probe for efficient circulating tumor cell detection on microfilter. *Biosensors and Bioelectronics*, 2022, 210: 114305. https://doi.org/10.1016/j.bios.2022.114305

[44] Y.J. Xie, L. Xu, J.H. Zhang, et al. Precise diagnosis of tumor cells and hemocytes using ultrasensitive, stable, selective cuprous oxide composite SERS bioprobes assisted with high-efficiency separation microfluidic chips. *Materials Horizons*, 2024, 11(22): 5752−5767. https://doi.org/10.1039/d4mh00791c

[45] G.C. Zheng, I. Pastoriza-Santos, J. Pérez-Juste, et al. Plasmonic metal-organic frameworks. *SmartMat*, 2021, 2(4): 446−465. https://doi.org/10.1002/smm2.1047
[46] L.E. Jamieson, S.M. Asiala, K. Gracie, et al. Bioanalytical measurements enabled by surface-enhanced Raman scattering (SERS) probes. *Annual Review of Analytical Chemistry*, 2017, 10: 415−437. https://doi.org/10.1146/annurev-anchem-071015-041557
[47] E. Papadopoulou, S.E.J. Bell. Label-free detection of single-base mismatches in DNA by surface-enhanced Raman spectroscopy. *Angewandte Chemie International Edition*, 2011, 50(39): 9058−9061. https://doi.org/10.1002/anie.201102776
[48] B.J. Hao, K.G. Wang, Y.K. Zhou, et al. Label-free detecting of the compaction and decompaction of ctDNA molecules induced by surfactants with SERS based on a nanoPAA-$ZnCl_2$-AuLs solid substrate. *ACS Omega*, 2020, 5(2): 1109−1119. https://doi.org/10.1021/acsomega.9b03294
[49] N.B. Yi, C. Zhang, Q.H. Song, et al. A hybrid system with highly enhanced graphene SERS for rapid and tag-free tumor cells detection. *Scientific Reports*, 2016, 6: 25134. https://doi.org/10.1038/srep25134
[50] Y.P. Xu, J. Lin, X.X. Wu, et al. A TiO_2-based bioprobe enabling excellent SERS activity in the detection of diverse circulating tumor cells. *Journal of Materials Chemistry B*, 2022, 10(20): 3808−3816. https://doi.org/10.1039/d2tb00464j
[51] T. Pan, D.H. Zhang, G.M. You, et al. PD-L1 targeted iron oxide SERS bioprobe for accurately detecting circulating tumor cells and delineating tumor boundary. *Chinese Chemical Letters*, 2025, 36(1): 109857. https://doi.org/10.1016/j.cclet.2024.109857
[52] J. Lin, D.H. Zhang, J. Yu, et al. Amorphous nitrogen-doped carbon nanocages with excellent SERS sensitivity and stability for accurate identification of tumor cells. *Analytical Chemistry*, 2023, 95(10): 4671−4681. https://doi.org/10.1021/acs.analchem.2c05272
[53] D.H. Zhang, J. Lin, Y.P. Xu, et al. A novel dual-function SERS-based identification strategy for preliminary screening and accurate diagnosis of circulating tumor cells. *Journal of Materials Chemistry B*, 2023, 11(40): 9666−9675. https://doi.org/10.1039/d3tb01545a
[54] Y.J. Xie, C. Chen, C.G. Zhang, et al. Synergistic enhancement of ultrahigh SERS activity *via* Cu_2O@Ag Core-Shell structure for accurate label-free identification of breast tumor
[55] L. Bottou. From machine learning to machine reasoning. *Machine Learning*, 2014, 94(2): 133−149. https://doi.org/10.1007/s10994-013-5335-x
[56] X.Y. Zhu, Y. Li, N. Gu. Application of artificial intelligence in the exploration and optimization of biomedical nanomaterials. *Nano Biomedicine and Engineering*, 2023, 15(3): 342−353. https://doi.org/10.26599/nbe.2023.9290035
[57] B.S.S. SivaRao, B.S. Rao. EfficientNet - XGBoost: An effective white-blood-cell segmentation and classification framework. *Nano Biomedicine and Engineering*, 2023, 15(2): 126−135. https://doi.org/10.26599/nbe.2023.9290014
[58] J. Plou, P.S. Valera, I. García, et al. Machine learning-assisted high-throughput SERS classification of cell secretomes. *Small*, 2023, 19(51): e2207658. https://doi.org/10.1002/smll.202207658
[59] X.F. Lu, J.L. Meng, H.T. Wang, et al. DNA replication stress stratifies prognosis and enables exploitable therapeutic vulnerabilities of HBV-associated hepatocellular carcinoma: An *in-silico* precision oncology strategy. *The Innovation Medicine*, 2023, 1(1): 100014. https://doi.org/10.59717/j.xinn-med.2023.100014
[60] W. Kong, J. Zhu, P.P. Shan, et al. iSKIN: Integrated application of machine learning and Mondrian conformal prediction to detect skin sensitizers in cosmetic raw materials. *SmartMat*, 2024, 5(6): e1278. https://doi.org/10.1002/smm2.1278
[61] Z.H. Sun, H. Yin, K.L. Liu, et al. Machine learning accelerated calculation and design of electrocatalysts for CO_2 reduction. *SmartMat*, 2022, 3(1): 68−83. https://doi.org/10.1002/smm2.1107
[62] M.A. Aslam, M.A. Munir, R. Ahmad, et al. Deep neural networks for prediction of cardiovascualr diseases. *Nano Biomedicine and Engineering*, 2022, 14(1): 81−89. https://doi.org/10.5101/nbe.v14i1.p81-89
[63] M. Greenacre, P.J.F. Groenen, T. Hastie, et al. Principal component analysis. *Nature Reviews Methods Primers*, 2022, 2(1): 100. https://doi.org/10.1038/s43586-022-00184-w
[64] S.P. Zhao, B. Zhang, J. Yang, et al. Linear discriminant analysis. *Nature Reviews Methods Primers*, 2024, 4: 70. https://doi.org/10.1038/s43586-024-00346-y
[65] X.L. Wu, Z.X. Liu, Y.X. Liu, et al. Construct high performance SERS sensing platform assisted by machine learning. *Alexandria Engineering Journal*, 2023, 81: 284−289. https://doi.org/10.1016/j.aej.2023.09.029
[66] T. Huang, H.Y. Xu, H.T. Wang, et al. Artificial intelligence for medicine: Progress, challenges, and perspectives. *The Innovation Medicine*, 2023, 1(2): 100030. https://doi.org/10.59717/j.xinn-med.2023.100030
[67] X.X. Wu, L.Q. Luo, S. Yang, et al. Improved SERS nanoparticles for direct detection of circulating tumor cells in the blood. *ACS Applied Materials & Interfaces*, 2015, 7(18): 9965−9971. https://doi.org/10.1021/acsami.5b02276
[68] W.H. Qian, M. Xing, M. Ye, et al. Reproducible and acid-responsive Rhodamine B/PEG functioned nanographene oxide-Au nanocomposites for surface-enhanced Raman scattering sensing. *SmartMat*, 2024, 5(6): e1305. https://doi.org/10.1002/smm2.1305
[69] T.S. Lan, D.X. Cui, T.Y. Liu, et al. Gold NanoStars: Synthesis, modification and application. *Nano Biomedicine and Engineering*, 2023, 15(3): 330−341. https://doi.org/10.26599/nbe.2023.9290025
[70] R. Yang, Y. Gao, Z.J. Ouyang, et al. Gold nanostar-based complexes applied for cancer theranostics. *View*, 2022, 3(3): 20200171. https://doi.org/10.1002/viw.20200171
[71] X.B. Mang, L.Q. Yao. Grazing-incidence small-angle X-ray scattering property of double-layered gold nanoparticle arrays. *Rare Metals*, 2022, 41(10): 3585−3590. https://doi.org/10.1007/s12598-016-0736-1
[72] X.B. Mang, L.Q. Yao. Hexagonal packing lattice formed by functionalized gold nanoparticles. *Rare Metals*, 2022, 41(11): 3858−3864. https://doi.org/10.1007/s12598-016-0744-1